Non-Volatile Reconfigurable Transmissive Notch Filter Using Wide Bandgap Phase Change Material Antimony Sulfide

Virat Tara, Rui Chen, Johannes E. Fröch, Zhuoran Fang, Jie Fang, Romil Audhkhasi, Minho Choi, and Arka Majumdar

(Invited Paper)

***Abstract*—Reconfigurable free-space metasurfaces with subwavelength-scale tunable nano-scatterers can manipulate light for many applications ranging from bio-medical imaging, light detection and ranging to optical computing. Several endeavors have been made to achieve tunable metasurfaces using thermo-optic, electro-optic effects, liquid crystals, and phase change materials (PCMs). PCMs stand out, particularly for low-tuning frequency and low-power consumption applications, thanks to their nonvolatile nature and drastic index modulation, leading to zero-static power and a small footprint. Antimony sulfide (Sb_2S_3) is an emerging low-loss PCM with the widest bandgap reported so far, enabling operation at low wavelengths down to ∼600 nm in the visible spectrum. In addition, Sb_2S_3 has slow crystallization speed, which enables amorphization of large-volume Sb_2S_3 without unintentional recrystallization. This makes Sb_2S_3 suitable for application in reconfigurable metasurfaces, where the switching area (usually > hundreds of μm^2) is significantly larger than photonic integrated circuits (tens of μm^2). Herein, we experimentally demonstrate an electrically tunable notch filter at a wavelength of ∼1150 nm on a Sb_2S_3-cladded silicon-on-sapphire platform. The notch filter is enabled by a 2-dimensional symmetry-protected quasi-bound-state-in-the-continuum (quasi-BIC) metasurface. We experimentally observed a quality factor of up to ∼200 and demonstrated reversible tuning of a record large volume (4.5 μm^3) of Sb_2S_3. Thanks to the large modulation provided by Sb_2S_3, we observed a resonance shift as high as ∼4 nm in situ using a doped silicon microheater. Our work paves the way for compact and low-power nonvolatile notch filters. Moreover, due to the low loss of Sb_2S_3 in the visible, this work also lays the foundation for phase-only modulation in the visible using PCMs.**

***Index Terms*—Antimony sulfide, bound states in the continuum, metasurface, notch filter, phase change material.**

Manuscript received 2 November 2023; revised 6 March 2024 and 16 June 2024; accepted 14 July 2024. Date of publication 18 July 2024; date of current version 7 August 2024. This work was supported in part by National Science Foundation under Grant NSF-1640986 and Grant NSF-2003509, in part by ONR-YIP Award, in part by DRAPER Labs, in part by DARPA-YFA Award, and in part by Intel. Part of this work was conducted at the Washington Nanofabrication Facility/ Molecular Analysis Facility, a National Nanotechnology Coordinated Infrastructure (NNCI) site at the University of Washington supported by the National Science Foundation under Award NNCI-1542101 and Award NNCI-2025489. *(Corresponding author: Virat Tara.)*

Virat Tara, Rui Chen, Johannes E. Fröch, Zhuoran Fang, Jie Fang, Romil Audhkhasi, and Minho Choi are with the Department of Electrical and Computer Engineering, University of Washington, Seattle, WA 98195 USA (e-mail: vtara@uw.edu).

Arka Majumdar is with the Department of Physics, University of Washington, Seattle, WA 98195 USA, and also with the Department of Electrical and Computer Engineering, University of Washington, Seattle, WA 98195 USA (e-mail: arka@uw.edu).

Color versions of one or more figures in this article are available at https://doi.org/10.1109/JSTQE.2024.3430214.

Digital Object Identifier 10.1109/JSTQE.2024.3430214

I. Introduction

Metasurfaces consisting of subwavelength scale nano-scatterer arrays can precisely manipulate light, finding numerous applications in bio-medical sensing [1], endoscopy [2], wireless communication [3], spectroscopy [4], light detection and ranging [5], and recently even optical computation and artificial intelligence [6], [7]. Post-fabrication reconfigurability [8] of such metasurfaces is generally desired and has been carried out using the thermo-optic effect [9], the electro-optic effect [10], liquid crystals (LCs) [11] or phase change materials (PCMs) [12], [13], [14], [15], [16], [17], [18], [19]. PCMs have numerous benefits over other approaches, primarily in that they provide nonvolatile and sizeable refractive index modulation upon transition between their amorphous(a)- and crystalline(c)-phases ($\Delta n \sim O(1)$ [13]). This leads to a "set-and-forget" operation with a compact device footprint critical for large-scale optical systems. Traditionally, PCMs such as $Ge_2Sb_2Te_5$ (GST) were mainly used in electronic memory applications and are sub-optimal for optical usage primarily because of their high absorptive losses in both a-, c- states in the visible or near-infrared (NIR) range. This precludes their usage for phase-only modulation in the NIR range and poses even more challenges to exploit them in the visible.

On the other hand, emerging wide bandgap PCM antimony sulfide (Sb_2S_3) [20] exhibits negligible optical loss both in its a- and c- states in the NIR spectrum. This emerging material provides an excellent solution to tuning any resonant structure without breaking desired resonant behavior, beyond the capability of GST. Furthermore, Sb_2S_3 is the only reversibly switchable PCM with low loss down to the visible spectrum (∼600 nm) reported so far, making it attractive for visible frequency metasurfaces. Besides all these advantages, the slow crystallization process of Sb_2S_3, as observed in this work and demonstrated previously in photonic integrated circuits [21], enables large area switching thanks to no unintentional recrystallization during the amorphization process. This is critical for free-space reconfigurable metasurfaces where the switching area (> thousands of μm^2) is generally much larger than integrated photonic circuits (tens of μm^2). Previous works on Sb_2S_3 have mainly relied on laser pulses to switch Sb_2S_3 [22], [23], [24], which is ex-situ and requires a well-aligned, bulky, and sophisticated pulsed laser setup, significantly limiting its usage. Although previous works demonstrated using ITO heaters [25] or doped silicon *p-i-n* heaters [21] to reversibly switch Sb_2S_3 in PICs, the challenge remains to switch a large volume of Sb_2S_3 for electrically reconfigurable metasurfaces.

Here, we experimentally demonstrate an electrically tunable notch filter based on a symmetry-protected quasi-BIC metasurface. The notch filter operates at a wavelength of ∼1150 nm on a Sb_2S_3-cladded silicon-on-sapphire platform via doped silicon microheaters. We experimentally observe a quality factor up to ∼200 and demonstrate reversible tuning of a large volume (∼4.5 μm^3) of Sb_2S_3. The device produced a resonance shift of up to ∼4 nm, amplitude attenuation of ∼40%, and an amplitude modulation of ∼30%. Non-volatile tunable notch filters are promising solutions to reconfigurable optical spectral filters with zero static power consumption. Moreover, they have strong potential for low-power displays [22], phase-only transmissive spatial light modulators [18], [26] and augmented reality displays which require localized dimming of selected pixels [12]. Our work paves the way for compact, low-power non-volatile notch filters.

II. Design of Reconfigurable Symmetry-Protected Quasi-BIC Metasurfaces

Fig. 1 shows our design of the 2-dimensional periodic metasurface, which supports a symmetry-protected BIC mode [27], [28], [29], [30]. Each unit cell contains two partially etched Si nano-bars, and the geometry and material layers are shown in Fig. 1(a)–(d). The periods along x- and y-directions (P_x and P_y) are 710 and 536 nm, respectively and the distance between the nano-bars was kept constant as 177.5 nm. The length, width (N_y and N_x) and height (H) of the nano-bars are 340, 110 and 240 nm, respectively. A doped silicon microheater is formed by keeping 100 nm (h) of Si un-etched underneath the metasurface. We optimize the microheater by adding a curvature on the edge to uniformly heat the metasurface and to switch a larger area of the PCM [31]. In contrast, a rectangular heater has much larger temperature gradients (Fig. 6) across the heating area, incurring a much higher temperature at the metasurface center and hence material ablation. This was also confirmed in the experiment (Fig. 7).

For normal incidence our device supports a BIC mode at a free-space wavelength of λ ∼1093 nm in case of the silicon only metasurface. For a rotation angle of 0° between the nanobars, the structure possesses a mirror symmetry along the x axis. The electric field profile (E_x) of the BIC mode is odd with respect to the mirror transformation $(y) \rightarrow (-y)$, while the incident illumination (x polarized) is even [32]. This mismatch prevents the mode from coupling to the incident radiation, causing it to

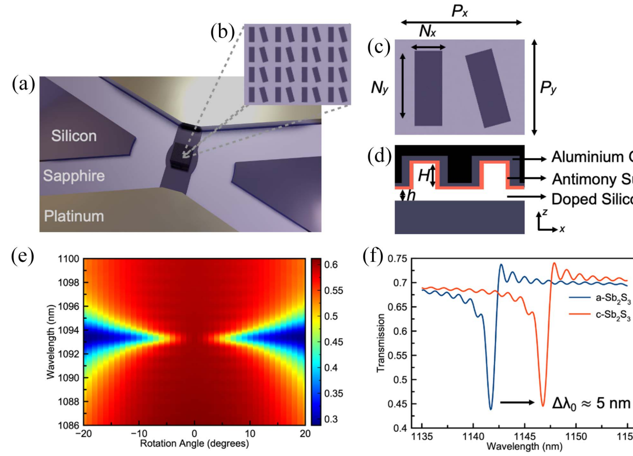

Fig. 1. Design of a symmetry-protected quasi-BIC meta surface. (a) Schematic of the device. (b) Zoomed-in schematic of the metasurface. (c) Zoomed-in schematic of a single unit cell. P_x and P_y denote the period of the metasurface in the x and y directions (710 nm and 536 nm, respectively). N_x and N_y denote the width and length of the nano-bars (340 nm and 110 nm), respectively. H is the height of the nano-bars, which was kept at 240 nm. h is the thickness of the partially etched silicon layer, kept at 100 nm. (d) Cross-section of a single unit cell showing different material layers. (e) Simulated transmission plot of silicon-only metasurface with respect to different wavelengths and rotation angles for x polarized incident illumination. The BIC mode is dark for an asymmetry factor of 0. The color bar represents the transmission value. (f) Simulated spectrum for both a- and c-Sb_2S_3. A resonance shift of ∼5 nm is observed for a quasi-BIC mode with an asymmetry parameter of 13°.

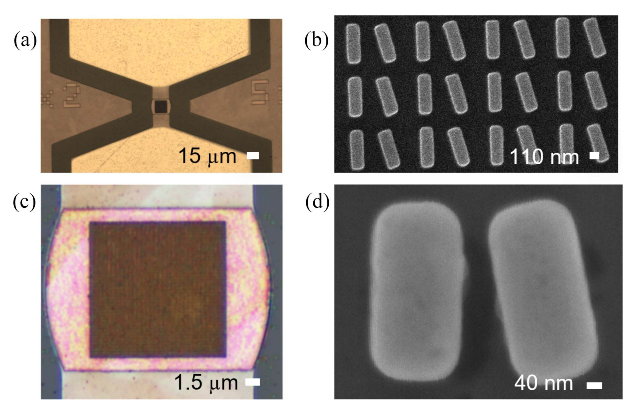

Fig. 2. Fabricated quasi-BIC metasurface (a) optical micrograph of the fabricated device. (Scale bar: 15 μm) (b) Zoomed-in image of the metasurface. (Scale bar: 110 nm) (b) scanning electron microscope (SEM) image of the silicon nano-bars. (Scale bar: 1.5 μm) (d) zoomed-in SEM image for a single unit cell after Sb_2S_3 and alumina deposition. (Scale bar: 40 nm).

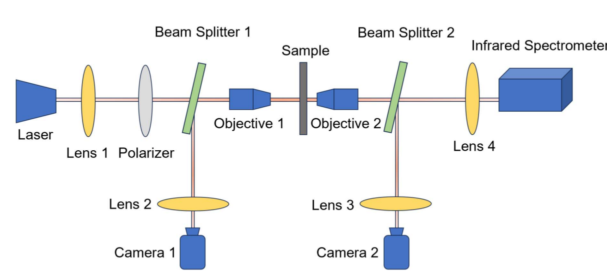

Fig. 3. Schematic of the setup used to characterize the fabricated sample.

have an infinite Q factor. This manifests itself in the absence of any resonance features in the transmission spectrum of the structure for a rotation angle of 0° (Fig. 1(e)). Breaking the in-plane mirror symmetry about the x axis by having a non-zero rotation angle instead of changing the incident angle [29] leads the field profile not being perfectly odd (see Figs. 8, 9 and 10) with respect to the same mirror symmetry leading to the coupling of the BIC mode to free-space radiation. This transforms the mode into a quasi-BIC mode with a finite resonance linewidth. The rotation angle governs the coupling rate of the mode to the radiative continuum spectrum, and therefore is an effective knob to tune the resonance linewidth of the notch-filter.

Reconfigurability is achieved by cladding the metasurface with 20 nm of Sb_2S_3 encapsulated by 40 nm of alumina. The encapsulation is crucial to protect the Sb_2S_3 from sulfur loss, oxidation and thermal reflowing during the high temperature phase transition process, hence reversible phase transitions [33]. Fig. 1(f) shows the simulated transmission spectrum for both a- and c-Sb_2S_3 and a large resonance shift of ∼5 nm is achieved with only 20 nm of Sb_2S_3. We picked this operation wavelength (∼1150 nm) to demonstrate the transparency of Sb_2S_3 at a relatively short wavelength, which is already beyond the capability of most of the prominent PCMs like GST and $Ge_2Sb_2Se_4Te_1$ (GSST) [12]. Moreover, the operating wavelength can be fine-tuned by scaling the unit cells uniformly (Fig. 11), providing a convenient way to design for different operation wavelengths.

III. Materials and Fabrication

A. Device Fabrication and Characterization Setups

The sample was fabricated from a 500-nm-silicon on sapphire (SOS) chip. The wafer was implanted by phosphorous ions with a dosage of 2×10^{15} ions per cm^2, ion energy of 40 keV and a tilt angle of 7°. It was then annealed at 950 °C (Expertech CTR200 Anneal Furnace) for 30 minutes to activate the dopants and to get a uniform dopant concentration of $\sim 10^{18}$ cm^{-3}. Then the silicon was thinned down to 340 nm using an inductively coupled plasma reactive ion etching etcher (ICP-RIE, Oxford Instruments PlasmaLab 100) with Fluorine gas chemistry. 300-nm-thick positive-tone E-beam resist (ZEP-520A) was then spin coated followed by a discharge layer (DisCharge H_2O). The resist was then patterned using E-beam lithography (JEOL JBX6300FS) and the pattern transferred onto the silicon layer using Fluorine-based ICP-RIE. After stripping the resist, Sb_2S_3 was deposited using DC sputtering (Lesker Sputter Lab 18) and immediately encapsulated with 40-nm Al_2O_3 using atomic layer deposition (Oxford Instruments PlasmaLab 80plus OpAl ALD). The sample was then annealed (Allin21 Corp Rapid Thermal Annealer - RTA) at 325 °C in Nitrogen environment for 10 minutes to crystallize the Sb_2S_3. Following this, negative photoresist (NR9G-3000PY) was spin coated onto the sample and patterned using direct laser writing lithography (Heidelberg DWL66+) to define the metal contacts. Before the metallization, Al_2O_3 and Sb_2S_3 were etched using a chlorine-based ICP-RIE etcher (Oxford Instruments PlasmaLab 100) to ensure an ohmic contact. Then, a room temperature DC sputterer (Evatec LLS EVO) was used to deposit Titanium/ Platinum (10/180 nm) followed by photoresist lift-off in acetone accompanied with

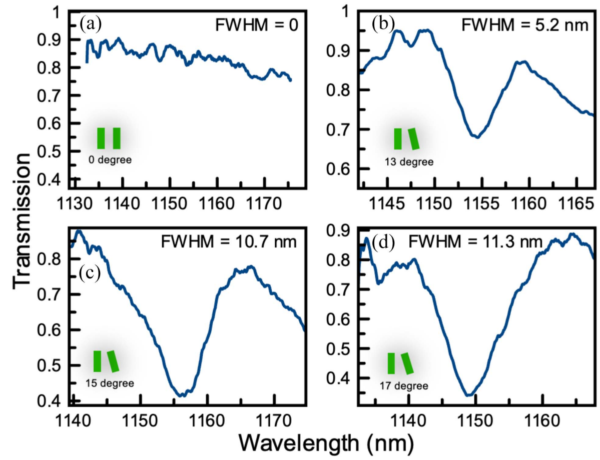

Fig. 4. Experimentally measured transmission spectrum of Sb_2S_3 cladded metasurface for rotation angle of (a) 0°, (b) 13°, (c) 15°, (d) 17° with Sb_2S_3 in the crystalline state. A direct dependence of the full-width-half-maximum (FWHM) on the rotation angle is observed, matching well with the simulation.

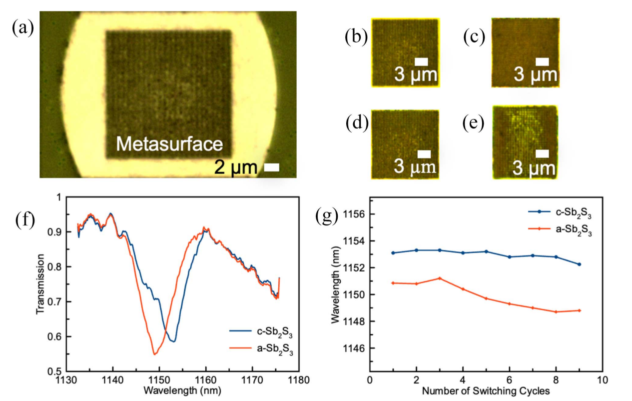

Fig. 5. Characterization results of the electrically reconfigurable metasurface. (a) A 15×15 μm^2 device on a curved doped silicon heater. (Scale bar: 2 μm) (b) Crystallized Sb_2S_3 after RTA at 325 °C. (Scale bar: 3 μm). (c) Amorphous Sb_2S_3 after a 20-V, 4-μs pulse, a visible change in color was seen between a- and c-Sb_2S_3. Also, a-Sb_2S_3 shows a more uniform color, in absence of white dot-like crystallites. (Scale bar: 3 μm). (d) c-Sb_2S_3 after 9-V DC voltage. (Scale bar: 3 μm). (e) Material ablated due to a 20-V, 15-μs pulse. (f) Transmission spectrum of the metasurface for a- and c-Sb_2S_3 at the 8^{th} cycle. The FWHM of the metasurface for a(c)-Sb_2S_3 is 8.7 (10.5) nm. (g) Extracted resonant wavelength for a- and c-Sb_2S_3 along 9 switching cycles, showing little performance degradation.

gentle sonication. In this case, sputtering was preferred over E-beam evaporation to avoid exposing the Sb_2S_3 to high temperatures, specifically temperatures above its ablation point. Finally, another step of direct laser writing lithography was performed to isolate the devices electrically with a positive-tone photoresist (AZ-1512). The silicon was then fully etched from the exposed areas using the Fluorine-based ICP-RIE etcher. Fig. 2 shows the micrographs and scanning electron microscope images of the fabricated device. Fig. 12 shows the diagram of various fabrication steps.

IV. Characterization of the Electrically Reconfigurable Metasurface

A. Setup

Fig. 3 shows the schematic of our measurement setup. The sample was illuminated using a broadband laser (WhiteLase

Micro). The laser light was first collimated using Lens 1, after which it was focused onto the sample using a 10× objective (Objective 1) of 0.26 numerical aperture (NA). The Dichroic Mirror 1 is used to deflect the reflected light from the metasurface to a camera (Camera 1 – Thorlabs CS165MU) along with an imaging lens (Lens 2). The transmitted light from the sample is collected using a 50× objective (Objective 2) with NA 0.65 and again split into an infrared camera (Camera 2 – Pembroke SenS SWIR) with imaging lens (Lens 3). Finally, the laser light is fiber coupled using Lens 4 and fed to the infrared sensor (Teledyne Pylon IR) and the spectrometer (Princeton Instruments Acton SpectraPro SP-2750). The electrical measurements were carried out using a pair of electrical probes on two probe positioners (Cascade Microtech DPP105-M-AI-S). The electrical pulses were generated from a arbitrary function generator (Keysight 81160 A).

B. Results

We first measure the spectrum of the devices to find the quasi-BIC mode. We observed the designed mode at ∼1150 nm. No measurable resonance was observed as shown in Fig. 4(a) for the device with rotation angle 0, indicating a dark BIC state. Whereas the asymmetrical devices in Fig. 4(b)–(d) produced a direct dependence of the FWHM with the rotation angle of the nano-bars, indicating a quasi-BIC state in excellent agreement with the simulation. We note that the quality factor is limited by fabrication imperfections and the high doping concentration of silicon ($\sim 10^{18}$ cm^{-3}) which adds extra absorption loss due to free-carrier dispersion effect (Fig. 13).

The amorphization process requires melting and quenching the Sb_2S_3 rapidly below its glass transition temperature, and the required cooling rate ($>1\ K \cdot ns^{-1}$) determines the area of Sb_2S_3 that can be switched reversibly. Here, we use a design of experiment approach to optimize the size of the meta surface - multiple devices of varying areas were fabricated on the same chip. Fig. 5(a) and (b) shows the microscope image of an as-fabricated c-Sb_2S_3 device of an area 15 × 15 μm^2 with the curved heater design. To change the Sb_2S_3 from c- to a-phase (amorphization), high-amplitude (20 V), relatively short duration (4 μs) electrical pulses were applied to produce a visual color change under the microscope in Fig. 5(c). After that, the sample was annealed under 325 °C for 10 mins to recrystallize Sb_2S_3, a similar microscope image as in Fig. 5(b) was observed, indicating that the Sb_2S_3 was switched reversibly. Later, crystallization was also induced electrically by applying a low amplitude (9 V), DC voltage. The micrograph after the applied crystallization voltage is shown in Fig. 5(d). The switching condition was then again verified by measuring the transmission spectrum of the metasurface. Ablated devices such as in Fig. 5(e) did not switch back due to the permanent material damage, hence no color change. We note that the high voltage requirement can be mainly attributed to the high resistance of our devices (∼200 ohms). This can be improved by further optimizing the doping profile and increasing the doped silicon microheater thickness. Additionally, the thermal performance can also be improved by changing the substrate material. Since sapphire has a much higher thermal conductivity ($\sim 30\ W/m \cdot K$) than SiO_2 ($\sim 1\ W/m \cdot K$) at room temperature, a higher heat dissipation in Al_2O_3 leads to inefficient heating. Therefore, replacing the substrate to SiO_2 or even suspending the metasurface membrane in air could significantly improve power efficiency.

Thanks to the uniform heating, 9 cycles of reversible switching were achieved with little performance degradation. Fig. 5(f) shows the measured transmission spectrum after 8 cycles. As expected, we observe a red-shift and Q-factor reduction after crystallization since c-Sb_2S_3 has a larger refractive index and absorptive loss (see Fig. 14). The losses of c-Sb_2S_3 can be mainly attributed to scattering of light due to the crystal grain boundaries, which can be minimized by reducing the grains size [34]. Furthermore, as c- to a- switching requires melting and rapid quenching of the material, quenching should be fast enough to avoid the onset of the crystallization process. Therefore, amorphization pulses in electro-thermal heaters are generally in the scale of hundreds of nanoseconds [35], [36]. However as observed in this work and previously reported [21], Sb_2S_3 can be switched from c- to a- state using >1 μs pulses. This indicates that the crystallization process in Sb_2S_3 is slower compared to PCMs such as GST [21], [35], leading to a much-relaxed critical cooling rate requirement and thus ability to switch large volume. The theoretical and practical upper limit of such a volume remains to be determined. We also show thermo-optic tuning of the resonance in Fig. 15. The thermal simulation results of a 20V 4 μs pulse are shown in Fig. 16. The tunable notch filter produced a resonance shift of up to ∼4 nm, amplitude attenuation of 2.5 dB at the resonance wavelength in amorphous state and an amplitude modulation of ∼30% due to PCM switching from a- to c- Sb_2S_3. The resonance wavelengths across 9 cycles are plotted in Fig. 5(g), showing little device degradation. A slight increase in the contrast can be attributed to a "conditioning" process for initial crystallite formation. We also characterized a larger device with an area of 20 × 16 μm^2 on a rectangular heater (Fig. 17). We were able to switch the device for 2 cycles. This demonstrates the difficulty of switching large volume Sb_2S_3 and we emphasize that this work showcases the largest Sb_2S_3 area (15 × 15 μm^2) that has been electrically and reversibly switched so far.

V. Conclusion

In summary, we have designed, fabricated, and experimentally demonstrated a reconfigurable non-volatile notch-filter based on a symmetry-protected quasi-BIC metasurface with high Q-factor of ∼200. The active modulation was provided by a 20-nm-thick layer of PCM Sb_2S_3, which was electrically controlled in situ by doped silicon microheaters. An amplitude attenuation of 2.5 dB and modulation of ∼30% was achieved at ∼1150 nm. We further showed reversible switching of large area of Sb_2S_3 (15 × 15 μm^2) up to 9 cycles with little performance degradation. In the future, we need to achieve lower voltage operation, higher extinction ratio, and larger number of switching cycles. Our work shows that wide-band gap PCMs are promising for phase-only modulations. Besides, due to low loss of Sb_2S_3 in the visible, this work also lays the foundation for applications of PCMs for phase-only modulation in visible-wavelength metasurfaces.

APPENDIX

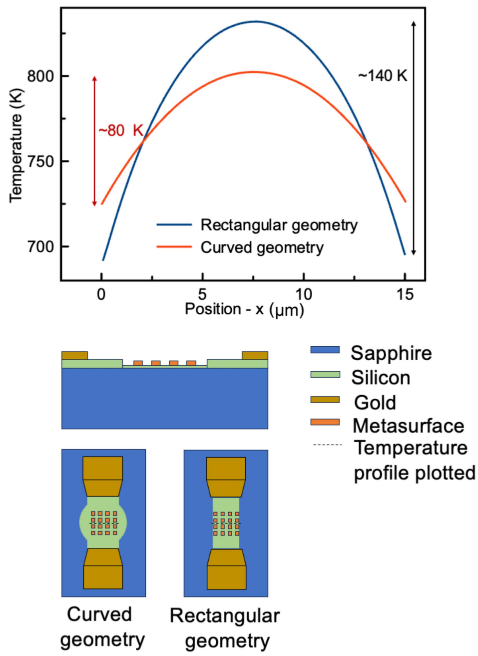

Fig. 6. 3D Thermal simulations for two different types of heater geometry. Compared to the rectangular geometry, the curved heater design can reduce the temperature variation from the edge to the center significantly, from 140 K to 80 K. The Silicon under the metal pads is 340 nm thick and under the metasurface the thickness if 100 nm.

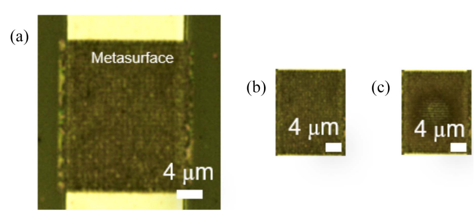

Fig. 7. Switching of 15x11 μm^2 device on a rectangular heater. (a) A 15 $\times$ 11 μm^2 device on a rectangular doped silicon heater. (Scale bar: 4 μm). (b) c-Sb_2S_3 after RTA at 325 °C. (Scale bar: 4 μm). (c) Visible material ablation after application of a 20V 4-μs electrical pulse. We attribute this to the concentration of very high temperature at the center of the device. (a) Micrograph of a 15 $\times$ 11 μm^2 device. (Scale bar: 4 μm).

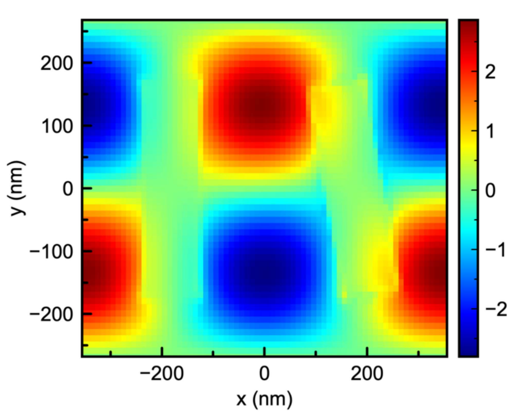

Fig. 8. E_x field profiles inside the unit cell at λ_0 ~1093 nm for asymmetry angle 13° in the case of silicon only metasurface. The simulation was performed using the Lumerical FDTD solver.

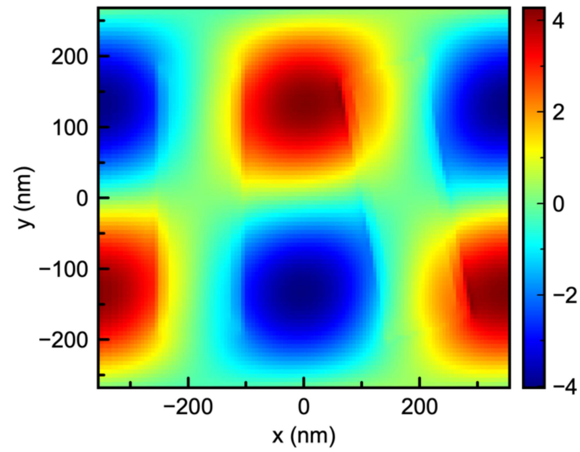

Fig. 9. Ex field profile inside the unit cell for asymmetry angle 13° and c-Sb_2S_3 at λ_0 ~1146 nm.

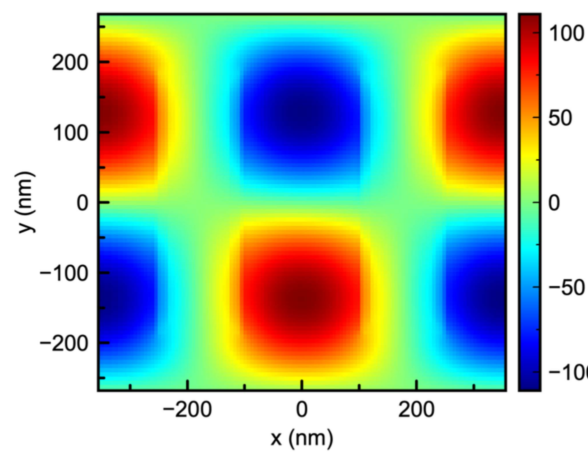

Fig. 10. Ex field profile inside the unit cell for asymmetry angle 0° and c-Sb_2S_3 at λ_0 ~ 1146 nm. The simulation was performed using a dipole cloud as the illumination source.

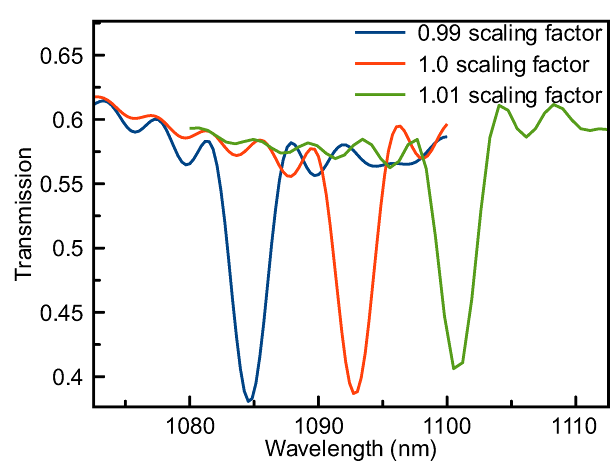

Fig. 11. Resonance wavelength for 3 different scaling factors in the case of the silicon only metasurface. A red(blue) shift occurs when increasing (decreasing) the size of the unit cell. A scaling factor of 0.99 means that all the dimensions of the unit cell in the *x*- and *y*- directions were multiplied by 0.99.

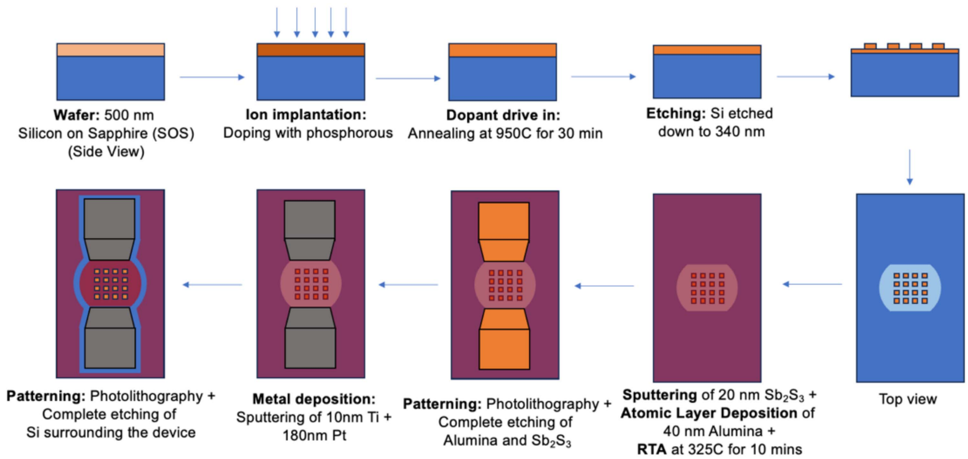

Fig. 12. The fabrication process flow Various steps followed to fabricate the reconfigurable metasurface.

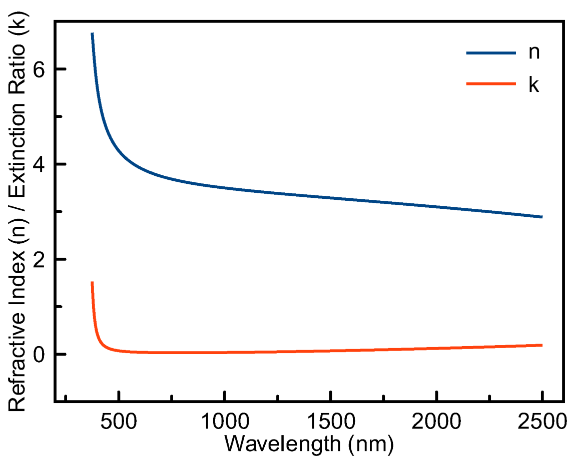

Fig. 13. Refractive index data of 230 nm doped Silicon on Sapphire measured using variable angle ellipsometry (woollam RC2).

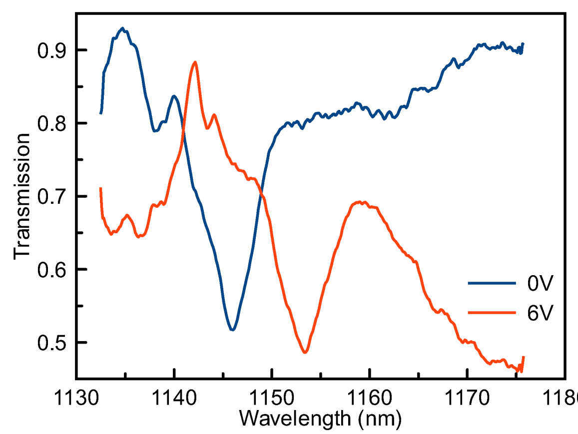

Fig. 15. Tuning via thermo-optic effect Change in the resonant wavelength of the Quasi-BIC mode after application of 6V DC due to thermo-optic effect.

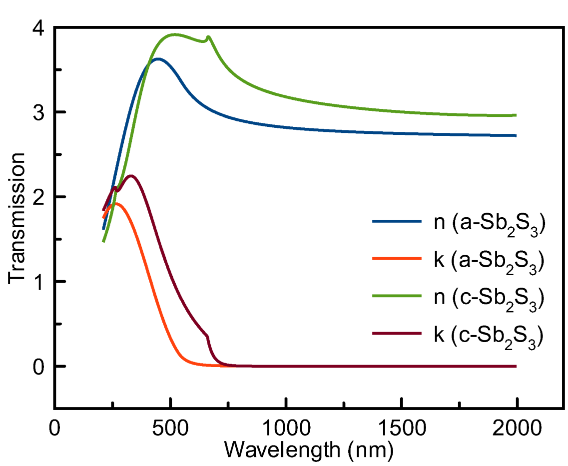

Fig. 14. Refractive index and extinction ratio values of 20 nm thick Sb_2S_3 used for simulations. The optical constants were measured using variable angle ellipsometer woollam RC2.

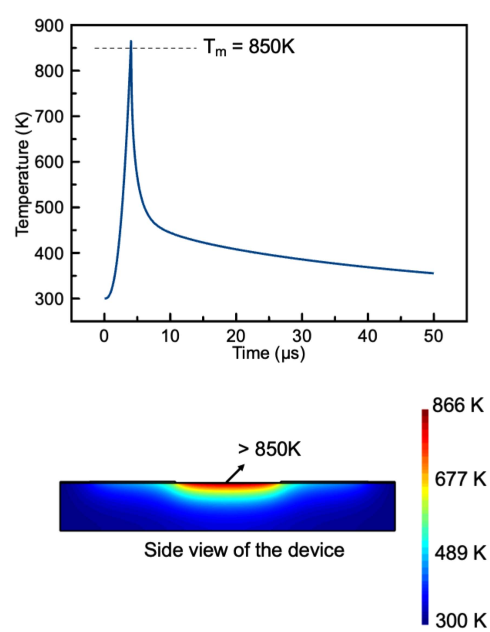

Fig. 16. 2D heat transfer simulation Plot and thermal distribution of a 20 V 4 μs pulse.

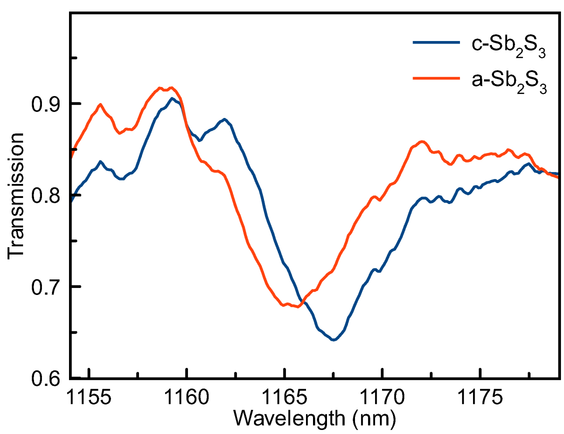

Fig. 17. Reversible tuning of a 20 × 16 μm^2 device for up to 2 cycles. Plot shows the 2nd cycle which had a resonance shift of ∼2 nm. A high voltage (20 V), 10 μs pulse was applied to switch the device. A relatively low-voltage (13 V) DC voltage was subsequently applied to re-crystallize Sb_2S_3.

REFERENCES

[1] A. Tittl et al., "Imaging-based molecular barcoding with pixelated dielectric metasurfaces," *Science*, vol. 360, pp. 1105–1109, 2018, doi: 10.1126/science.aas9768.

[2] J. E. Fröch et al., "Real time full-color imaging in a meta-optical fiber endoscope," *eLight*, vol. 3, 2023, Art. no. 13, doi: 10.1186/s43593-023-00044-4.

[3] J. C. Zhang et al., "A 6G meta-device for 3D varifocal," *Sci. Adv.*, vol. 9, 2023, Art. no. eadf8478, doi: 10.1126/sciadv.adf8478.

[4] R. Wang et al., "Compact multi-foci metalens spectrometer," *Light Sci. Appl.*, vol. 12, 2023, Art. no. 103, doi: 10.1038/s41377-023-01148-9.

[5] R. Juliano Martins et al., "Metasurface-enhanced light detection and ranging technology," *Nature Commun.*, vol. 13, 2022, Art. no. 5724, doi: 10.1038/s41467-022-33450-2.

[6] M. K. Chen, X. Liu, Y. Sun, and D. P. Tsai, "Artificial intelligence in meta-optics," *Chem. Rev.*, vol. 122, no. 19, pp. 15356–15413, Oct. 2022, doi: 10.1021/acs.chemrev.2c00012.

[7] L. Huang, S. Mukherjee, Q. Tanguy, J. Fröch, and A. Majumdar, "Photonic advantage of optical encoders," in *Proc. 2023 Conf. Lasers Electro-Opt.*, San Jose, CA, USA, 2023, pp. 1–2.

[8] T. Gu et al., "Reconfigurable metasurfaces towards commercial success," *Nature Photon.*, vol. 17, pp. 48–58, 2023, doi: 10.1038/s41566-022-01099-4.

[9] M. Bosch, M. R. Shcherbakov, Z. Fan, and G. Shvets, "Polarization states synthesizer based on a thermo-optic dielectric metasurface," *J. Appl. Phys.*, vol. 126, 2019, Art. no. 073102.

[10] G. K. Shirmanesh, R. Sokhoyan, P. C. Wu, and H. A. Atwater, "Electro-optically tunable multifunctional metasurfaces," *ACS Nano*, vol. 14, no. 6, pp. 6912–6920, Jun. 2020, doi: 10.1021/acsnano.0c01269.

[11] T. Badloe et al., "Liquid crystal-powered Mie resonators for electrically tunable photorealistic color gradients and dark blacks," *Light Sci. Appl.*, vol. 11, 2022, Art. no. 118, doi: 10.1038/s41377-022-00806-8.

[12] Z. Fang, R. Chen, V. Tara, and A. Majumdar, "Non-volatile phase-change materials for programmable photonics," *Sci. Bull.*, vol. 68, no. 8, pp. 783–786, Apr. 2023, doi: 10.1016/j.scib.2023.03.034.

[13] R. Chen et al., "Opportunities and challenges for large-scale phase-change material integrated electro-photonics," *ACS Photon.*, vol. 9, no. 10, pp. 3181–3195, Oct. 2022, doi: 10.1021/acsphotonics.2c00976.

[14] L. Mao, Y. Li, G. Li, S. Zhang, and T. Cao, "Reversible switching of electromagnetically induced transparency in phase change metasurfaces," *Proc. SPIE*, vol. 2, no. 5, Oct. 2020, Art. no. 056004, doi: 10.1117/1.AP.2.5.056004.

[15] C. Ríos et al., "Ultra-compact nonvolatile phase shifter based on electrically reprogrammable transparent phase change materials," *PhotoniX 3*, vol. 26, 2022. [Online]. Available: https://doi.org/10.1186/s43074-022-00070-4

[16] T. Cao et al., "Multi-cycle reconfigurable THz extraordinary optical transmission using chalcogenide metamaterials," *Opto-Electron. Sci.*, vol. 1, no. 1, Nov. 2021, Art. no. 210010, doi: 10.29026/oes.2022.210010.

[17] K. Liu et al., "Non-volatile dynamically switchable color display via chalcogenide stepwise cavity resonators," *Opto-Electron. Adv.*, vol. 7, 2024, Art. no. 230033, doi: 10.29026/oea.2024.230033.

[18] Z. Fang et al., "Nonvolatile phase-only transmissive spatial light modulator with electrical addressability of individual pixels," *ACS Nano*, vol. 18, no. 17, pp. 11245–11256, Apr. 2024, doi: 10.1021/acsnano.4c00340.

[19] R. E. Simpson, J. K. W. Yang, and J. Hu, "Are phase change materials ideal for programmable photonics?: Opinion," *Opt. Mater. Exp.*, vol. 12, no. 6, pp. 2368–2373, Jun. 2022, doi: 10.1364/OME.456895.

[20] M. Delaney, I. Zeimpekis, D. Lawson, D. W. Hewak, and O. L. Muskens, "A new family of ultralow loss reversible phase-change materials for photonic integrated circuits: Sb_2S_3 and Sb_2Se_3," *Adv. Funct. Mater.*, vol. 30, 2020, Art. no. 2002447, doi: 10.1002/adfm.202002447.

[21] R. Chen et al., "Non-volatile electrically programmable integrated photonics with a 5-bit operation," *Nature Commun.*, vol. 14, no. 1, Jun. 2023, Art. no. 3465, doi: 10.1038/s41467-023-39180-3.

[22] H. Liu et al., "Rewritable color nanoprints in antimony trisulfide films," *Sci. Adv.*, vol. 6, 2020, Art. no. eabb7171, doi: 10.1126/sciadv.abb7171.

[23] P. Moitra et al., "Programmable wavefront control in the visible spectrum using low-loss chalcogenide phase-change metasurfaces," *Adv. Mater.*, vol. 35, 2023, Art. no. 2205367, doi: 10.1002/adma.202205367.

[24] K. Gao et al., "Intermediate phase-change states with improved cycling durability of Sb_2S_3 by femtosecond multi-pulse laser irradiation," *Adv. Funct. Mater.*, vol. 31, 2021, Art. no. 2103327, doi: 10.1002/adfm.202103327.

[25] Z. Fang et al., "Non-volatile reconfigurable integrated photonics enabled by broadband low-loss phase change material," *Adv. Opt. Mater.*, vol. 9, 2021, Art. no. 2002049, doi: 10.1002/adom.202002049.

[26] S.-Q. Li et al., "Phase-only transmissive spatial light modulator based on tunable dielectric metasurface," *Science*, vol. 364, no. 6445, pp. 1087–1090, Jun. 2019, doi: 10.1126/science.aaw6747.

[27] K. Koshelev, S. Lepeshov, M. Liu, A. Bogdanov, and Y. Kivshar, "Asymmetric metasurfaces with high-Q resonances governed by bound states in the continuum," *Phys. Rev. Lett.*, vol. 121, no. 19, Nov. 2018, Art. no. 193903, doi: 10.1103/PhysRevLett.121.193903.

[28] Y. Zhang et al., "Active optical modulation of quasi-BICs in Si–VO_2 hybrid metasurfaces," *Opt. Lett.,*, vol. 47, pp. 5517–5520, 2022.

[29] N. J. J. van Hoof et al., "Unveiling the symmetry protection of bound states in the continuum with terahertz near-field imaging," *ACS Photon.*, vol. 8, no. 10, pp. 3010–3016, Oct. 2021, doi: 10.1021/acsphotonics.1c00937.

[30] S. Li, C. Zhou, T. Liu, and S. Xiao, "Symmetry-protected bound states in the continuum supported by all-dielectric metasurfaces," *Phys. Rev. A*, vol. 100, no. 6, Dec. 2019, Art. no. 063803, doi: 10.1103/PhysRevA.100.063803.

[31] Y. Zhang et al., "Electrically reconfigurable non-volatile metasurface using low-loss optical phase-change material," *Nature Nanotechnol.*, vol. 16, pp. 661–666, 2021, doi: 10.1038/s41565-021-00881-9.

[32] J. D. Joannopoulos, S. G. Johnson, J. N. Winn, and R. D. Meade, *Photonic Crystals: Molding the Flow of Light (Second Edition)*, 2nd ed. Princeton, NJ, USA: Princeton Univ. Press, 2008.

[33] R. Chen et al., "Opportunities and challenges for large-scale phase-change material integrated electro-photonics," *ACS Photon.*, vol. 9, no. 10, pp. 3181–3195, 2022.

[34] J. Li et al., "Performance limits of phase change integrated photonics," *IEEE J. Sel. Topics Quantum Electron.*, vol. 30, no. 4, Jul./Aug. 2024, Art. no. 6100109, doi: 10.1109/JSTQE.2024.3360526.

[35] R. Chen et al., "Broadband nonvolatile electrically controlled programmable units in silicon photonics," *ACS Photon.*, vol. 9, no. 6, pp. 2142–2150, Jun. 2022, doi: 10.1021/acsphotonics.2c00452.

[36] Z. Fang et al., "Ultra-low-energy programmable non-volatile silicon photonics based on phase-change materials with graphene heaters," *Nature Nanotechnol.*, vol. 17, no. 8, pp. 842–848, Aug. 2022, doi: 10.1038/s41565-022-01153-w.

Virat Tara received the B.E. degree in electronics and communications from Thapar University-Patiala, Patiala, India, in 2017, and the master's degree in 2023 from the University of Washington, Seattle, WA, USA, where he is currently working toward the Ph.D. degree with the Department of Electrical and Computer Engineering. His research interests include nano-photonics and reconfigurable optical metasurfaces.

Rui Chen received the B.S. degree in optoelectronic information science and engineering from Zhejiang University, Zhejiang, China, in 2018, and the M.S. degree in electrical engineering from Columbia University, New York, NY, USA, in 2020. Since then, he has been working toward the Ph.D. degree with the University of Washington, Seattle, WA, USA. His research interests include programmable integrated photonics and metasurfaces using phase-change materials.

Johannes E. Fröch received the B.Sc. and M.Sc. degrees from the Technical University of Graz, Graz, Austria, in 2014 and 2016, respectively, and the Ph.D. degree from the University of Technology, Sydney, NSW, Australia, in 2021. He is currently a Postdoctoral Researcher with the Department of Electrical and Computer Engineering, University of Washington, Seattle, WA, USA. His research interests include nanophotonics and their applications.

Zhuoran Fang received the Master of Engineering degree from University of Oxford, Oxford, U.K., and the Ph.D. degree in electrical engineering from the University of Washington, Seattle, WA, USA. He was with Hewlett Packard Labs and Meta Reality Labs. His research focuses on nonvolatile programmable silicon photonics based on phase-change materials.

Jie Fang received the B.E. degree in opto-electronics information science and engineering from Fudan University, Shanghai, China, in 2018, and the Ph.D. degree in materials science and engineering from the University of Texas at Austin, Austin, TX, USA, in 2023. He is currently a Postdoctoral Scholar with the Nano Optoelectronic Integrated System Engineering Lab, Department of Electrical and Computer Engineering, University of Washington, Seattle, WA, USA. His research interests include nanophotonics, meta-optics, excitonic physics, and photonic integrated circuits.

Romil Audhkhasi received the bachelor’s degree in applied physics from the Indian Institute of Technology, Delhi, New Delhi, India, and the Ph.D. degree in electrical engineering from the University of Southern California, Los Angeles, CA, USA. He is currently a Postdoctoral Scholar with Prof. Arka Majumdar’s Lab, University of Washington, Seattle, WA, USA. His research interests include designing microphotonic devices for applications in imaging, cryptography, and thermal emission control.

Minho Choi received the doctorate degree in the field of semiconductor quantum photonics from the Department of Physics, Korea Advanced Institute of Science and Technology, Daejeon, South Korea, in 2022. He is currently conducting research in the areas of nano-photonics and optical implementation of neural networks with the University of Washington, Seattle, WA, USA.

Arka Majumdar received the B.Tech. degree from the Indian Institute of Technology Kharagpur, Kharagpur, India, in 2007, where he was honored with the President’s Gold Medal, and the M.S. and Ph.D. degrees in electrical engineering from Stanford University, Stanford, CA, USA, in 2009 and 2012, respectively. He is currently an Associate Professor with the Departments of Electrical and Computer Engineering and Physics, University of Washington, Seattle, WA, USA. He spent one year with the University of California, Berkeley, CA, USA during 2012–2013 as a Postdoc before joining Intel Labs during 2013–2014. His research interests include developing a hybrid nanophotonic platform using emerging material systems for optical information science, imaging, and microscopy.